

# Search for New Physics in Events with Jets and Missing Transverse Momentum at the CMS Experiment

Dissertation

zur Erlangung des Doktorgrades

des Fachbereichs Physik

der Universität Hamburg

vorgelegt von

Dipl.- Phys. Kristin Goebel geb. Heine

aus Gifhorn

Hamburg

2014



Gutachter der Dissertation:	Prof. Dr. bla Prof. Dr. bla
Gutachter der Disputation:	Prof. Dr. bla Prof. Dr. bla
Datum der Disputation:	?? . ?? 2014
Vorsitzender des Prüfungsausschusses:	Dr. bla
Vorsitzender des Promotionsausschusses:	Prof. Dr. bla
Leiterin des Fachbereichs Physik:	Prof. Dr. bla
Dekan der Fakultät für Mathematik, Informatik und Naturwissenschaften:	Prof. Dr. bla



## Abstract

bla

## Kurzfassung

bla



# Contents

<b>1</b>	<b>Introduction</b>	<b>1</b>
<b>2</b>	<b>Theoretical Background</b>	<b>2</b>
2.1	The Standard Model of Particle Physics . . . . .	2
2.1.1	Limitations of the Standard Model . . . . .	2
2.2	Supersymmetry . . . . .	2
2.2.1	Searches for Supersymmetry at Collider Experiments . . . . .	2
<b>3</b>	<b>Experimental Setup</b>	<b>3</b>
3.1	The Large Hadron Collider . . . . .	3
3.2	The CMS Experiment . . . . .	4
3.2.1	Coordinate Conventions and Kinematic Variables . . . . .	6
3.2.2	Superconducting Magnet . . . . .	6
3.2.3	Inner Tracking System . . . . .	6
3.2.4	Electromagnetic Calorimeter . . . . .	8
3.2.5	Hadron Calorimeter . . . . .	9
3.2.6	Muon System . . . . .	11
3.2.7	Trigger System . . . . .	12
3.3	Data Taking and Event Simulation . . . . .	12
<b>4</b>	<b>Object Reconstruction and Particle Identification</b>	<b>13</b>
4.1	Global Event Description with the Particle-Flow Algorithm at CMS . . . . .	13
4.2	Reconstruction of Jets . . . . .	13
4.2.1	Jet Algorithms . . . . .	13
4.2.2	Jet Types at CMS . . . . .	13
4.2.3	Jet Energy Calibration . . . . .	13
4.3	Identification of Boosted Top Quark Decays . . . . .	13
4.3.1	The CMS Top Tagger . . . . .	13
4.3.2	The HEP Top Tagger . . . . .	13
<b>5</b>	<b>Measurement of the Jet Transverse-Momentum Resolution</b>	<b>14</b>
5.1	Basic Concept of the Dijet Asymmetry Method . . . . .	14
5.2	Applcation to Realistic Collision Events . . . . .	14
5.3	Samples and Event Selection . . . . .	14
5.3.1	Datasets and Triggers . . . . .	14
5.3.2	Selection Criteria . . . . .	14
5.4	Corrections to the Dijet Asymmetry . . . . .	14
5.4.1	Correction for Additional Jet Activity . . . . .	14
5.4.2	Correction for Particle-Level Imbalance . . . . .	14
5.4.3	Results of the Corrections to the Asymmetry . . . . .	14



5.5	Determination of the Data-to-Simulation Ratio . . . . .	14
5.6	Validation of the Method . . . . .	14
5.6.1	Validation in Simulated Events . . . . .	14
5.6.2	Validation of the Measured Data-to-Simulation Ratio . . . . .	14
5.7	Systematic Uncertainties . . . . .	14
5.8	Extension of the Method to the Forward Detector Region . . . . .	14
5.9	Results . . . . .	14
5.9.1	Comparison to Other Measurements . . . . .	14
<b>6</b>	<b>Search for New Physics with Jets and Missing Transverse Momentum</b>	<b>15</b>
6.1	Event Selection . . . . .	15
6.1.1	Data samples and trigger . . . . .	15
6.1.2	Event Cleaning . . . . .	15
6.1.3	Baseline Selection . . . . .	15
6.1.4	Exclusive Search Regions . . . . .	15
6.2	QCD Background Estimation with the Rebalance-And-Smear Method . . .	15
6.2.1	Rebalance Procedure using Kinematic Fits . . . . .	15
6.2.2	Response Smearing . . . . .	15
6.2.3	Validation Tests . . . . .	15
6.2.4	Systematic Uncertainties . . . . .	15
6.2.5	QCD Background Prediction . . . . .	15
6.3	Estimation of Non-QCD Backgrounds . . . . .	15
6.3.1	Invisible Z Background . . . . .	15
6.3.2	Hadronic $\tau$ Background . . . . .	15
6.3.3	Lost-Lepton Background . . . . .	15
6.4	Results and Interpretation . . . . .	15
<b>7</b>	<b>Prospect Studies for a Search for Top Squarks at <math>\sqrt{s} = 13</math> TeV</b>	<b>16</b>
7.1	Data samples . . . . .	16
7.2	Top Tagging Efficiency Studies . . . . .	16
7.2.1	Top Tag Efficiency . . . . .	16
7.2.2	Misidentification Rate . . . . .	16
7.3	Studies towards a Suitable Analysis Strategy . . . . .	16
7.4	Results and Discussion . . . . .	16
7.4.1	Comparison of the Performance of Various Selections . . . . .	16
7.4.2	Discussion of Specific Simplified Assumptions in the Analysis . . . .	16
<b>8</b>	<b>Conclusions</b>	<b>17</b>

# 1 Introduction

blabla bla [1]

## **2 Theoretical Background**

### **2.1 The Standard Model of Particle Physics**

#### **2.1.1 Limitations of the Standard Model**

### **2.2 Supersymmetry**

#### **2.2.1 Searches for Supersymmetry at Collider Experiments**

## 3 Experimental Setup

In order to probe the various aspects of the well-established standard model or search for hints of new physics beyond the SM, particle physics experiments preferentially make use of powerful particle accelerators where particles of a certain type are collided in order to probe the constituents of matter and interactions between them. The analyses presented in this thesis are all performed in the context of the CMS experiment located at the Large Hadron Collider (LHC) at CERN near Geneva.

The first part of this chapter provides an introduction to the LHC. This is followed by an overview of the detector system of the CMS experiment. Afterwards the hitherto periods of collision data taking at the LHC are discussed together with an introduction to the generation of simulated events which are used in the analysis of real data events.

### 3.1 The Large Hadron Collider

The Large Hadron Collider [2,3] is a ring-accelerator designed to provide particle collisions of hadrons. It is built in the tunnel of the former LEP [4] collider 45 – 170 m below the ground and has a circumference of 26.7 km. The LHC is a particle-particle collider and thus composed of two rings with counter-rotating beams. The operation can be performed in different modes with either proton beams or heavy ions like e.g. lead <sup>1</sup>.

In each beam, protons are grouped together in bunches and accelerated in two evacuated beam pipes using superconducting radio-frequency cavities. With a nominal bunch spacing of 25 ns the bunch revolution frequency is 40 MHz. Each of the 2808 individual bunches per beam contains at design conditions  $1.15 \times 10^{11}$  protons. In order to bend the beams around the LHC ring superconducting dipole magnets are used with an operation temperature of 1.9 K. They provide a magnetic field of up to 8.33 T while additional quadrupole and sextupole magnets are utilized to squeeze and focus the beams.

Before the protons are injected into the LHC they are already pre-accelerated in various smaller accelerators up to a beam energy of 450 GeV while passing through the injector chain Linac2 – Proton Synchrotron Booster (PSB) – Proton Synchrotron (PS) – Super Proton Synchrotron (SPS). An overview of the accelerator complex at CERN is given in Fig. 3.1.

The main goal of the LHC is to provide proton-proton collisions to the experiments with center of mass energies up to 14 TeV in order to explore physics processes at novel energy regimes. The expected number of events  $N$  for a certain type of process is given by the product of the specific cross section  $\sigma$  of that process and the integral  $L = \int \mathcal{L} dt$  of the instantaneous luminosity  $\mathcal{L}$  over time such that

$$N = \sigma \cdot L. \tag{3.1}$$

---

<sup>1</sup>All studies presented in this thesis are based on proton-proton collisions. Thus the operation with heavy ions is not discussed.

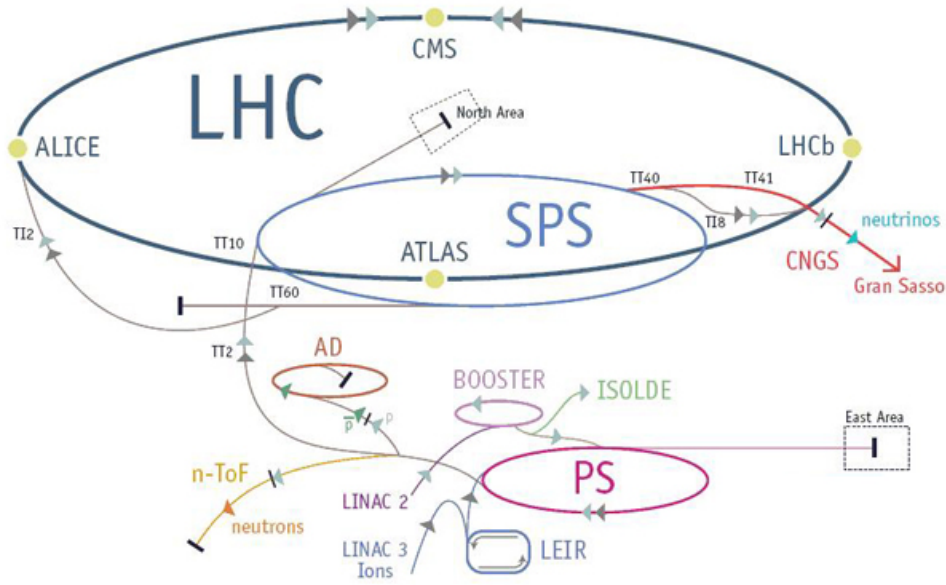


Figure 3.1: Illustration of the CERN accelerator complex including the injector chain of the LHC ring. Taken from [5].

The luminosity is a machine parameter and can be expressed for beams with Gaussian-shaped profiles as

$$\mathcal{L} = \frac{f n_1 n_2}{4\pi\sigma_x\sigma_y} \cdot F \quad (3.2)$$

with the revolution frequency  $f$ , the number of particles  $n_1$  and  $n_2$  contained in the two colliding bunches and the transverse beam sizes  $\sigma_x$  ( $\sigma_y$ ) in the horizontal (vertical) directions. In order to take the inclination of the two beams into account, the geometrical correction factor  $F$  is introduced. The nominal peak luminosity of the LHC is  $10^{34} \text{ cm}^{-2} \text{ s}^{-1}$ .

The LHC beams cross at four locations along the ring. At these interaction points the four main experiments of the LHC are located in order to measure the delivered particle collisions. The two high luminosity experiments ATLAS [6] and CMS [7,8] are designed for multiple purposes like precision measurements of SM quantities, search for the standard model Higgs Boson or searches for signals indicating new physics processes. The LHCb detector [9] however is a specialised experiment focusing on the measurement of CP violation in the interactions of hadrons containing b-quarks. The only experiment designed especially for the analysis of heavy ion collisions is the ALICE [10] detector with the main emphasis on the physics of strongly interacting matter at extreme energy densities like for instance quark-gluon plasma.

### 3.2 The CMS Experiment

The CMS detector is one of the two experiments at the LHC designed to address a multitude of physics questions. In addition to tests of the SM at the TeV scale, studies of the nature of elektroweak symmetry breaking which might show up in the presence of a Higgs

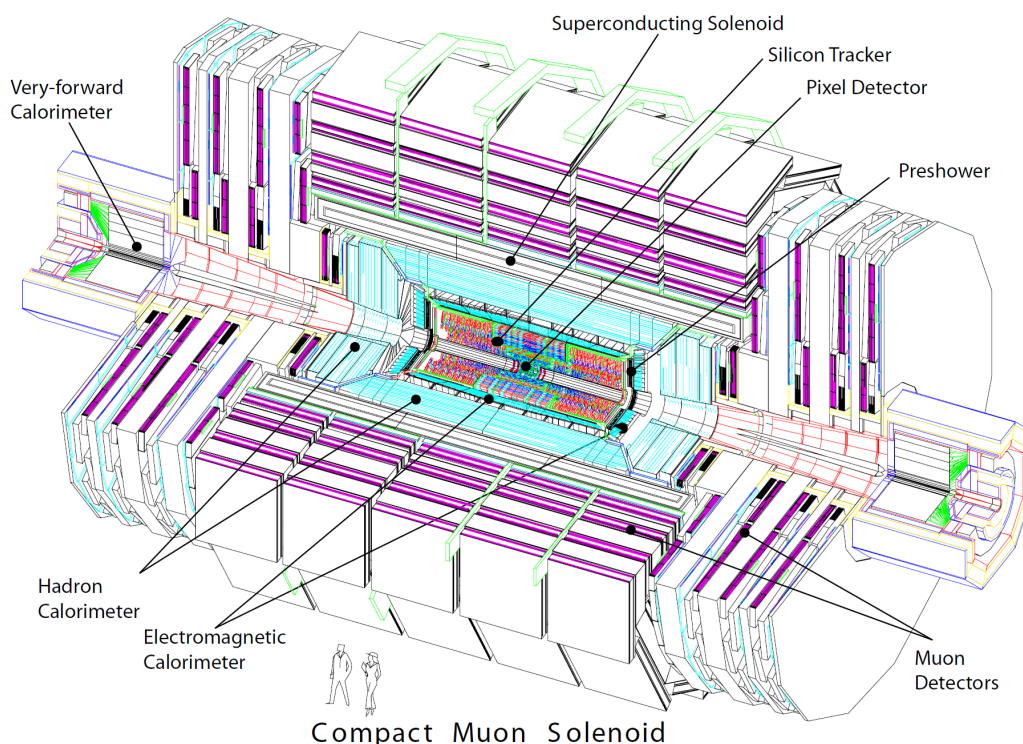


Figure 3.2: A perspective view of the CMS detector [7].

boson and searches for so far unknown particles pointing to e.g. new symmetries in nature are the primary targets of these experiments. These ambitious physics goals can only be achieved by fully exploiting the by now unprecedented collision energy and luminosity. Since the total inelastic proton-proton cross-section at a center of mass energy of 14 TeV is expected to be around 100 mb, the experiments have to deal with an event rate of approximately  $10^9$  events per second. This is resulting in high experimental challenges. The CMS detector with its typical cylindrical design of different sub-detector components around the beam line is designed to perfectly meet these particular conditions. A sketch of the CMS detector and the different sub-detectors is shown in Fig. 3.2. As a typical high-energy particle experiment the CMS detector makes mainly use of tracking detectors and calorimeters to measure particles' momenta, energy depositions and flight directions in order to identify the objects emerging from the particle collisions. Table ... gives an overview of the performance goals of the various sub-detectors. The overall dimension of the CMS detector are a length of 21.6 m and a diameter of 14.6 m resulting in a total weight of 12500 t.

The following sections comprise a description of the CMS detector and individual sub-detector components focusing on the detector parts most relevant for the analyses presented in this thesis. A detailed discussion of the detector design can be found in [7, 8].

Bild +  
Ref

Performance  
Table

### 3.2.1 Coordinate Conventions and Kinematic Variables

In order to describe the particle collisions, the CMS experiment makes use of a right-handed coordinate system with its origin at the center of the detector at the nominal interaction point. While the z-axis is defined along the direction of the beam, the x-axis points to the center of the LHC ring and the y-axis vertically upwards. In this xy-plane the azimuthal angle  $\phi$  is measured where  $\phi = 0$  coincides with the x-axis. The polar angle  $\theta$  however is defined with respect to the z-axis. A quantity closely related to the polar angle is the pseudorapidity  $\eta$  defined as

$$\eta = -\ln \left[ \tan \left( \frac{\theta}{2} \right) \right] \quad (3.3)$$

which is widely used in experimental particle physics as rapidity differences are Lorentz invariant. A pseudorapidity  $\eta = 0$  corresponds to the direction perpendicular to the beam while  $|\eta| \rightarrow \infty$  points along the beam. Based on the pseudorapidity the Lorentz invariant distance between two objects  $\Delta R$  can be written as

$$\Delta R = \sqrt{(\Delta\eta)^2 + (\Delta\phi)^2}. \quad (3.4)$$

At the LHC the initial conditions of the primary collisions are not known as the specific energy fraction of the proton which each parton carries can not be identified. Thus conservation of the total momentum can not be utilized directly to describe the momentum balance in the final state. However, it is known that the initial particles have no significant momentum orthogonal to the beam axis which is referred to as transverse momentum

$$p_T = p \cdot \sin\theta. \quad (3.5)$$

Thus, momentum conservation in the transverse plane is used to describe the final state conditions. Any difference between the total sum of all transverse momenta and zero is considered as missing energy  $\cancel{E}_T$  and often exploited to describe undetected particles.

### 3.2.2 Superconducting Magnet

The CMS experiment makes use of a large superconducting solenoid magnet which is a crucial component of the whole detector design and provides a magnetic field of up to 4 T. It allows to precisely determine the momenta and charge of charged particles from the bended tracks that they follow in the magnetic field.

With a length of 12.5 m and a diameter of the free bore of 6.3 m the total cold mass reaches 220 t. It is made up of a niobium-titanium coil which is wound in 4-layers. This configuration allows a storage of 2.6 GJ energy at full current. A 10000 t heavy-weight iron yoke is responsible for the return of the magnetic flux.

### 3.2.3 Inner Tracking System

The tracking system of the CMS experiment is the innermost part of the detector and installed directly around the interaction point completely contained in the bore of the magnet system. Its' purpose is to precisely measure the trajectories of charged particles arising from the collisions as well as to reconstruct secondary vertices. Due to the location

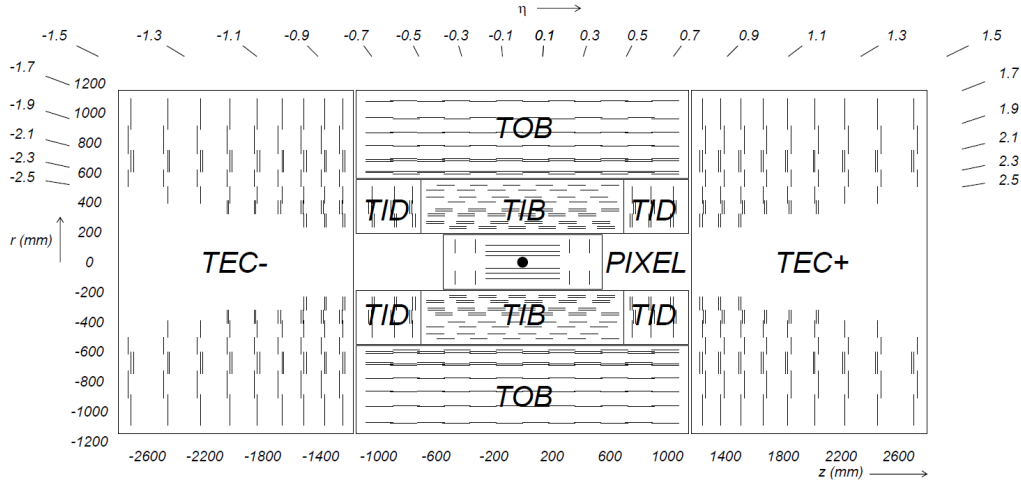


Figure 3.3: Sketch of the CMS tracking system in a  $rz$ -view. Each tracker module is represented by one line. Taken from [7].

close to the interaction point the tracking system has to cope with a high particle flux crossing the tracker associated with each bunch crossing. Hence high requirements on response time and granularity are set in order to properly identify the particles' tracks. In order to fulfill these tasks the CMS experiment makes use of a tracker design based on silicon detectors. It consists of mainly two components: the innermost part is made of silicon pixel detectors while these are surrounded by silicon strip modules. In total they add up to an active area of  $200 \text{ m}^2$  with a length of  $5.8 \text{ m}$  and a diameter of  $2.5 \text{ m}$  covering the detector up to  $|\eta| = 2.5$ . A schematic overview of the whole tracking system is shown in Fig. 3.3.

**Pixel Detector:** The pixel detector consists of three barrel layers which extend from  $4.4 \text{ cm}$  to  $10.2 \text{ cm}$  and two endcap disks on each side. In total there are 1440 pixel modules installed. The size of one pixel cell is  $100 \times 150 \mu\text{m}^2$  providing similar track resolution quality in  $r - \phi$  and  $z$  direction. This configuration provides for almost the whole range up to  $|\eta| = 2.5$  three precise tracking hits. This is especially important for the reconstruction of secondary vertices.

**Silicon Strip Tracker:** The silicon strip detector which extends to a radius of  $1.1 \text{ m}$  comprises the pixel tracker. The more than 15000 individual strip detector modules are arranged in an inner and an outer detector part. The inner part of the strip tracker is build by the four Tracker Inner Barrel (TIB) layers which are accompanied by the three Tracker Inner Disks (TID) at the end sides. This inner part provides up to four track measurements in the  $r - \phi$  plane. The TIB/TID system lies within the Tracker Outer Barrel (TOB) consisting of another six barrel layers while it is complemented by the Tracker EndCaps (TEC) which add another nine disks at each side of the tracking system. This layout provides at least around nine hits within the silicon strip system.

The tracking system with the design described above provides a very good impact parameter resolution and tracking efficiency [11]. The impact parameter resolution is of the



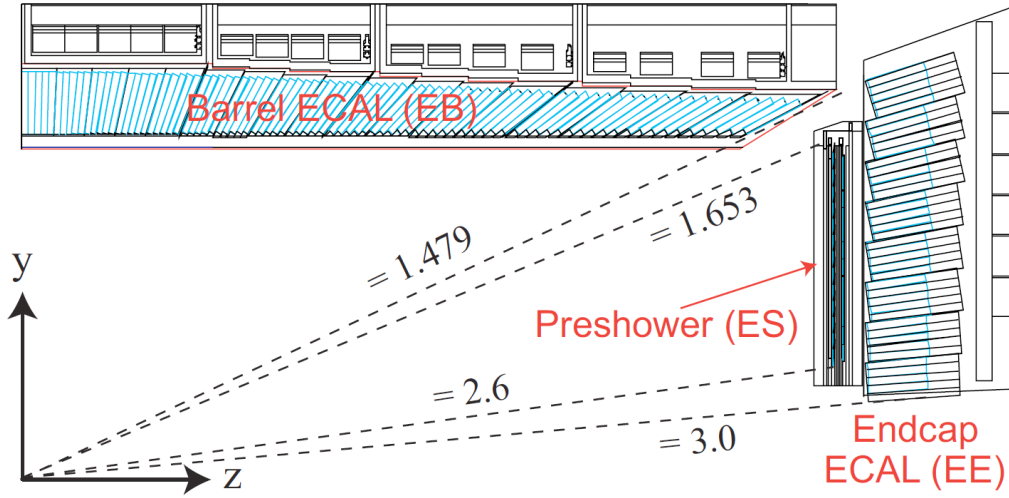


Figure 3.4: View of one quarter section of the CMS electromagnetic calorimeter in a  $yz$ -view. Taken from [8].

order of  $< 35 \mu\text{m}$  in the plane perpendicular to the beam (for particles with  $p_T > 10 \text{ GeV}$ ) and reaches  $75 \mu\text{m}$  in the longitudinal direction. Also the track reconstruction efficiency is expected to show a very good performance. The reconstruction efficiency of high energetic electrons is above 90%, that of charged hadrons up to 95% (for  $p_T > 10 \text{ GeV}$ ) and that for muons even better than 98% in the whole covered region up to  $|\eta| = 2.5$  already for muons with very low transverse momenta around  $1 \text{ GeV}$ .

### 3.2.4 Electromagnetic Calorimeter

The CMS experiment makes use of a homogeneous electromagnetic calorimeter (ECAL) in order to precisely measure the energy deposits of electrons and photons. It is installed around the inner tracking system covering a range up to  $|\eta| = 3.0$  and consists of lead tungstate ( $\text{PbWO}_4$ ) crystals. These have been chosen as they provide a high density, short radiation length and a small Molière radius and hence allow to build a compact calorimeter with a fine granularity. As 80% of the scintillation light is emitted within 25 ns, this matches well the bunch crossing rate of the LHC machine. In order to collect the radiated light photodiodes are glued to the back of each crystal.

An overview of the ECAL layout is shown in Fig. 3.4. The individual sub-components are the following:

**Barrel ECAL (EB):** The barrel detector of the ECAL covers the pseudorapidity region up to  $|\eta| = 1.479$ . Within a radius of about  $1.3 \text{ m}$  a total number of 61200 crystals are installed. Each of them has a length of  $230 \text{ mm}$  resulting in a radiation length of  $25.8 X_0$ . Avalanche photodiodes are used to detect the emitted scintillation light.

**Endcap ECAL (EE):** The EB is complemented on each side by an endcap which consists of two d-shaped halves. The ECAL endcaps extend from  $|\eta| = 1.479$  to  $|\eta| = 3.0$ . In total they contain another 14648 crystals with an individual length of

220 mm corresponding to  $24.7 X_0$ . For the collection of scintillation light vacuum phototriodes are used in the endcaps.

**Preshower (ES):** In front of the endcap crystals a preshower detector is placed. It covers the pseudorapidity range of  $|\eta| = 1.653 - 2.6$ . The main purpose is to identify photons emerging from the decay of neutral pions. It is a two-layer sampling calorimeter with lead as absorber material and silicon strip sensors measuring the deposited energy. The total thickness of the preshower is 20 cm ( $3 X_0$ ).

In order to achieve a stable and uniform energy measurement across the whole ECAL an accurate calibration is of crucial importance. In addition to the calibration of the absolute energy scale especially channel-to-channel effects – referred to as intercalibration – have to be accounted for. This intercalibration is mainly done based on physics events as e.g.  $\pi^0 \rightarrow \gamma\gamma$  or  $W \rightarrow e\nu$ . Changes in the transparency of the ECAL crystals during operation caused by irradiation are monitored by a dedicated laser system injecting well defined laser pulses into the crystals via optical fibres.

### 3.2.5 Hadron Calorimeter

In addition to the previously described electromagnetic calorimeter, the calorimetry of the CMS experiment is completed by the hadron calorimeter (HCAL). It is designed to provide an accurate energy measurement of hadron jets and indirectly also of invisible particles like e.g. neutrinos by the determination of missing transverse energy. In order to obtain a measure of the missing transverse energy it is important that the calorimeter is hermetic in the sense that it provides a large geometric coverage to potentially measure all particles emerging from an interaction. Thus the HCAL is build such that a pseudorapidity range up to  $|\eta| = 5.2$  is comprised.

The hadron calorimeter completely surrounds the inner tracking system and the electromagnetic barrel calorimeter while it is mainly contained within the magnet system. Hence its radial dimensions are limited on the one hand by the outer circumference of the barrel ECAL and on the other hand by the inner border of the magnet coil. To ensure that the complete hadronic showers are contained in the HCAL, an additional calorimeter component is installed outside the solenoid in the barrel part.

An overview of the layout of the CMS hadron calorimeter is shown in Fig. 3.5. It is a typical sampling calorimeter with alternating layers of absorber material and active scintillator layers. The individual sub-components are the following:

**Hadron barrel (HB):** The barrel part of the CMS hadron calorimeter covers the pseudorapidity range up to  $|\eta| = 1.3$  and is composed of two half barrels each containing 36 identical azimuthal wedges. These wedges hold the absorber plates which are flat brass plates arranged parallel to the axis of the beam. For reasons of stability the first and last layers are made of stainless steel. The total thickness of the absorber material ranges from 5.82 interaction lengths ( $\lambda_I$ ) at  $|\eta| = 0.0$  to  $10.6 \lambda_I$  at  $|\eta| = 1.3$ . The 17 active plastic scintillator layers alternate with the absorber plates and have a segmentation in  $(\Delta\eta, \Delta\phi)$  of  $(0.087, 0.087)$ . Each half barrel is divided into 16  $\eta$ -regions for which the individual tiles are optically linked together using wavelength shiftig fibres and thus form so-called *HCAL towers*. The read-out of each longitudinal tower is carried out using pixelated hybrid photodiodes.

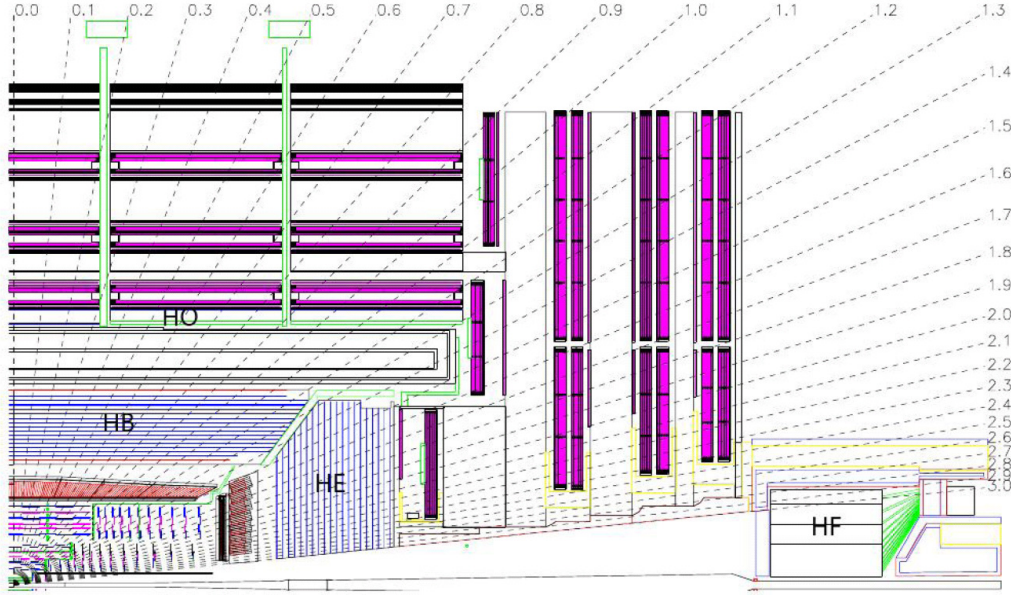


Figure 3.5: Longitudinal view of one quarter of the CMS detector showing the location of the individual HCAL sub-detector parts. Taken from [7].

**Hadron outer (HO):** The calorimeters in the central pseudorapidity region do not provide a sufficient depth in order to fully contain all hadronic showers. Therefore the HB is complemented by the outer hadron barrel part which is placed outside the solenoid covering  $|\eta| \leq 1.26$ . The HO makes use of the solenoid as additional absorber material and adds another one or even two layers in the most central part of scintillators to the barrel region. Thus the total depth is extended to  $11.8 \lambda_I$ .

**Hadron endcap (HE):** The hadron barrel calorimeter is supplemented by the hadron endcap. It is mounted on the endcap iron yoke and covers the pseudorapidity region of  $1.3 \leq |\eta| \leq 3.0$  using 18 scintillator layers inserted into brass absorber plates. The granularity of the endcap calorimeter is the same as for the barrel up to  $|\eta| = 1.6$  and gets coarser for larger pseudorapidities with  $(\Delta\eta, \Delta\phi) \approx (0.17, 0.17)$ .

**Hadron forward (HF):** The forward hadron calorimeter extends the pseudorapidity coverage from  $|\eta| = 2.9$  (slightly overlapping with the HE) up to  $|\eta| = 5.2$ . It is located 11.2 m from the nominal interaction point and has to be in particular radiation hard to cope with the vast particle flux. Thus the HF is made of steel absorber plates with radiation hard quartz fibres integrated as active material. These fibres are arranged parallel to the beam line and form towers with a size in  $(\Delta\eta, \Delta\phi)$  of  $\approx (0.175, 0.175)$ . The signal is detected as Cerenkov light originating from the quartz fibres.

Similar to the ECAL also the performance of the HCAL has to be well calibrated and further monitored during operation. Thus an initial calibration using a radioactive source is combined with test beam data to derive the absolute energy scale. A continuous update of this calibrations is performed using isolated energetic particles e.g. from decays of W

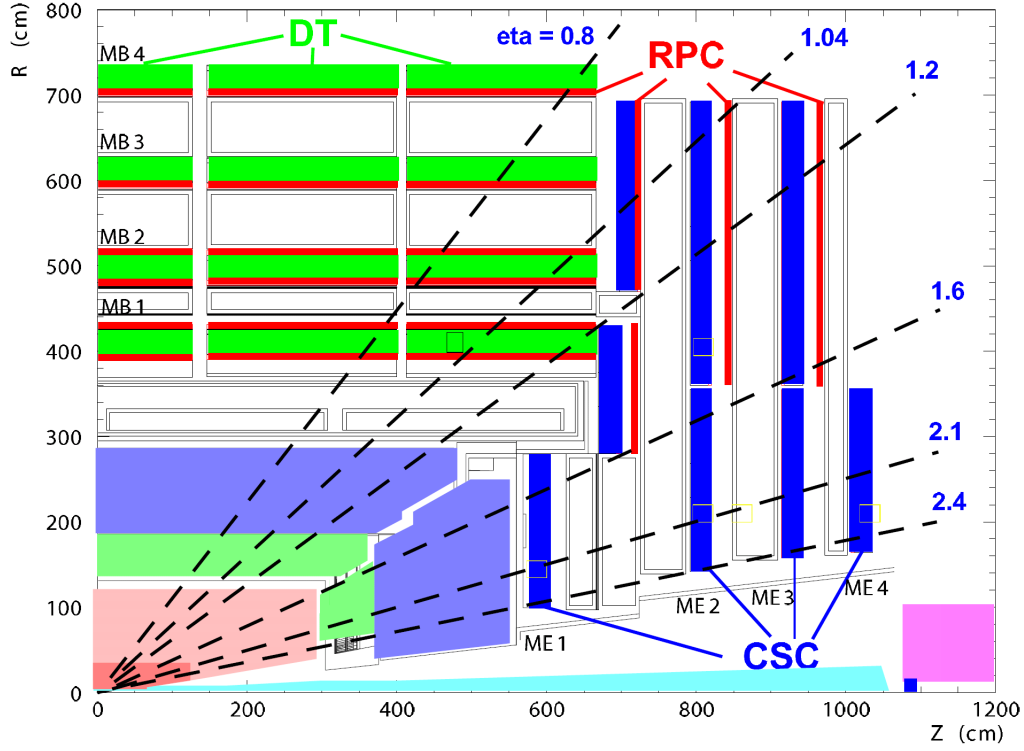


Figure 3.6: Taken from [8].

or Z bosons. In order to perform a fast monitoring various techniques like for instance a UV-laser system are exploited.

### 3.2.6 Muon System

The outermost part of the CMS detector – as seen from the interaction point – is made up of the muon system. This important component of the detector is assembled in the return yoke of the CMS magnet and consists of a central barrel cylinder which is complemented by endcap disks in the forward region. This results in a coverage of the pseudorapidity range up to  $|\eta| = 2.4$ . In the barrel part four layers of detectors are installed alternating with the iron yoke while the detectors in the endcap are mounted on four discs perpendicular to the beam. In total about  $25000\text{ m}^2$  detection planes are employed. The layout of the muon system is illustrated in Fig. 3.6.

In order to feature a good muon momentum resolution given the different radiation conditions and variations in the homogeneity of the magnetic field depending on the pseudorapidity region it is made use of three different types of gaseous detectors. These different types of tracking chambers are described in the following:

**Drift tube (DT) chambers:** In the barrel region for  $|\eta| < 1.2$  where the background due to neutrons is low and residual effects from the magnetic field likewise the muon system is equipped with drift tube chambers. While in all four stations in the barrel the muon coordinates in the  $r\phi$ -plane are measured, only the first three layers provide also a measurement of the  $z$ -direction. The maximum drift length was

chosen to be 21 mm resulting in a negligible occupancy while keeping the number of active channels at an acceptable level. Furthermore, a technology based on tubes was chosen avoiding the issue of possibly broken wires. The resolution in  $r\phi$  is designed to reach a precision of  $100\ \mu\text{m}$ .

**Cathode strip chambers (CSC):** The endcap regions are equipped with cathode strip chambers and cover the pseudorapidity range  $0.9 < |\eta| < 2.4$ . These are chosen as they provide a fast response time and fine segmentation while they are resistant against radiation. Thus they are well suited for the forward region where the muon and background rates are largely increased and the magnetic field is high and non-uniform. The CSCs which are multiwire proportional chambers where anode wires are interlaced with cathode panels perform a precise position measurement in the  $r\phi$  bending plane with a spatial resolution of  $75\text{--}150\ \mu\text{m}$ .

**Resistive plate chambers (RPC):** Resistive plate chambers are used to complement the drift tube and cathode strip chambers in the range  $|\eta| < 1.6$ . These are gaseous parallel-plate detectors with a spacial resolution coarser than the DTs and CSCs but usable at high particle rates while providing a very fast response and good time resolution. Thus they are able to very efficiently detect the correct bunch-crossing a muon track is associated to.

The global muon reconstruction efficiency is in general about 95 – 99% and only drops for some  $|\eta|$  regions like e.g. in the transition region between the barrel and endcap part around  $|\eta| = 1.2$ . Since muons reaching the muon system are affected by multiple scattering the resolution for muons with low transverse momenta below  $\approx 200\ \text{GeV}$  is in general better based on the inner tracking system than for the muon system alone. For highly energetic muons it is comparable. In general, the muon momentum resolution can be improved by combining the information from the inner tracker and the muon system due to an improved fault finding.

### 3.2.7 Trigger System

## 3.3 Data Taking and Event Simulation

## **4 Object Reconstruction and Particle Identification**

### **4.1 Global Event Description with the Particle-Flow Algorithm at CMS**

### **4.2 Reconstruction of Jets**

#### **4.2.1 Jet Algorithms**

#### **4.2.2 Jet Types at CMS**

#### **4.2.3 Jet Energy Calibration**

### **4.3 Identification of Boosted Top Quark Decays**

#### **4.3.1 The CMS Top Tagger**

#### **4.3.2 The HEP Top Tagger**

# **5 Measurement of the Jet Transverse-Momentum Resolution**

## **5.1 Basic Concept of the Dijet Asymmetry Method**

## **5.2 Application to Realistic Collision Events**

## **5.3 Samples and Event Selection**

### **5.3.1 Datasets and Triggers**

### **5.3.2 Selection Criteria**

## **5.4 Corrections to the Dijet Asymmetry**

### **5.4.1 Correction for Additional Jet Activity**

### **5.4.2 Correction for Particle-Level Imbalance**

### **5.4.3 Results of the Corrections to the Asymmetry**

## **5.5 Determination of the Data-to-Simulation Ratio of the Jet Transverse Momentum Resolution**

## **5.6 Validation of the Method**

### **5.6.1 Validation in Simulated Events**

### **5.6.2 Validation of the Measured Data-to-Simulation Ratio**

## **5.7 Systematic Uncertainties**

## **5.8 Extension of the Method to the Forward Detector Region**

## **5.9 Results**

### **5.9.1 Comparison to Other Measurements**

# **6 Search for New Physics in the Multijet and Missing Transverse Momentum Final State at $\sqrt{s} = 8$ TeV**

## **6.1 Event Selection**

### **6.1.1 Data samples and trigger**

### **6.1.2 Event Cleaning**

### **6.1.3 Baseline Selection**

### **6.1.4 Exclusive Search Regions**

## **6.2 QCD Background Estimation with the Rebalance-And-Smear Method**

### **6.2.1 Rebalance Procedure using Kinematic Fits**

### **6.2.2 Response Smearing**

### **6.2.3 Validation Tests**

### **6.2.4 Systematic Uncertainties**

### **6.2.5 QCD Background Prediction**

## **6.3 Estimation of Non-QCD Backgrounds**

### **6.3.1 Invisible Z Background**

### **6.3.2 Hadronic $\tau$ Background**

### **6.3.3 Lost-Lepton Background**

## **6.4 Results and Interpretation**



## **7 Prospect Studies for a Search for Top Squarks in Events with Jets and Missing Transverse Momentum at $\sqrt{s} = 13$ TeV**

### **7.1 Data samples**

### **7.2 Top Tagging Efficiency Studies**

#### **7.2.1 Top Tag Efficiency**

#### **7.2.2 Misidentification Rate**

### **7.3 Studies towards a Suitable Analysis Strategy**

### **7.4 Results and Discussion**

#### **7.4.1 Comparison of the Performance of Various Selections**

#### **7.4.2 Discussion of Specific Simplified Assumptions in the Analysis**

## 8 Conclusions

bla

# Bibliography

- [1] K. Nakamura and et al. (Particle Data Group), “Review of particle physics”, *J. Phys. G* **37** (2010, and 2011 partial update for the 2012 edition) 075021. doi:10.1088/0954-3899/37/7A/075021.
- [2] O. S. Brüning, P. Collier, P. Lebrun et al., “LHC Design Report”, volume 1: The LHC Main Ring. CERN, Geneva, 2004. CERN-2004-003-V-1.
- [3] L. Evans and P. Bryant, “LHC Machine”, *Journal of Instrumentation* **3** (2008), no. 08, S08001. doi:10.1088/1748-0221/3/08/S08001.
- [4] CERN, “LEP Design Report”, volume 2: The LEP Main Ring. CERN, Geneva, 1984. CERN-LEP-84-01.
- [5] CERN, “LHC: the guide (English version)”. CERN-Brochure-2009-003-Eng, 2009.
- [6] ATLAS Collaboration, “The ATLAS Experiment at the CERN Large Hadron Collider”, *JINST* **3** (2008) S08003. doi:10.1088/1748-0221/3/08/S08003.
- [7] CMS Collaboration, “The CMS experiment at the CERN LHC”, *JINST* **3** (2008) S08004. doi:10.1088/1748-0221/3/08/S08004.
- [8] CMS Collaboration, “CMS Detector Performance and Software”, volume 1 of *CMS Physics Technical Design Report*. CERN, Geneva, 2006. CMS-TDR-008-1. CERN-LHCC-2006-001.
- [9] LHCb Collaboration, “The LHCb Detector at the LHC”, *JINST* **3** (2008) S08005. doi:10.1088/1748-0221/3/08/S08005.
- [10] ALICE Collaboration, “The ALICE experiment at the CERN LHC”, *JINST* **3** (2008) S08002. doi:10.1088/1748-0221/3/08/S08002.
- [11] CMS Collaboration, “The CMS tracker system project”, volume 5 of *Technical Design Report CMS*. CERN, Geneva, 1997. CMS-TDR-005. CERN-LHCC-98-006.

